Modelling the micro-damage process zone during cortical bone fracture

Daniel Dapaah[a], Raphael Badaoui[a,c], Aram Bahmani[b], John Montesano[a,b], Thomas Willett[a,b,*]

[a] *Systems Design Engineering, University of Waterloo, 200 University Ave. W., Waterloo, Canada*
[b] *Mechanical and Mechatronics Engineering, University of Waterloo, 200 University Ave. W., Waterloo, Canada*
[c] *Bio-Mechanics and Bio-Engineering, Université de Technologie Compiègne, rue Roger Coutolenc, 60205 Compiègne, France*

ABSTRACT

Cortical bone employs intrinsic toughening mechanisms to delay crack growth initiation and propagation hence increasing its fracture toughness. Computational models of the bone fracture process though do not explicitly capture these intrinsic local toughening mechanisms. Such models could provide insights into possible sub-microscale mechanisms involved in the bone fracture process. Therefore, in this study, the intrinsic toughening mechanism referred to as the micro-damage process zone (MDPZ) was modelled using a bi-linear continuum damage law. This model was then experimentally validated using single edge notch bending specimens and digital image correlation for strain field measurements. The size and shape of the micro-damage process zone as well as the load-deflection curves generated by the model reasonably replicated those measured experimentally. The results indicate that the continuum damage mechanics approach is a robust means of modelling the MDPZ at the continuum level and with further development of the model can provide a useful tool for studies of the fracture process in cortical bone.

1. Introduction

The quest for greater mechanistic understanding of the damage and fracture behaviour of bone, which is of great clinical significance, has led to the development of many computational models of bone fracture. Bone, a natural composite material combines hydroxyapatite crystals, proteins and, in a lesser proportion, water, to form a complex multi-scale organised structure [1]. During the fracture process of bone, which is characterised by the propagation of a macroscopic crack, this multi-scale structure is engaged [2,3]. To better understand these interactions that exist between the multi-scale structure, the characteristics and properties of bone (mainly cortical bone) and the propagation of cracks to fracture, computational models of cortical bone fracture have been developed. These models provide a simpler means of investigating the fracture process of bone to further supplement findings made experimentally [4]. Further, they may provide insights into mechanisms that may be at play in the fracture process which might be difficult to determine experimentally. Different approaches and theorems have been applied such as the extended finite element method [5–7], cohesive finite element modelling [8–11] and molecular dynamics [12,13] in building these models. These models have been used to investigate the role of the volume fraction and arrangement of the bone crystals [3,4], crosslinking of bone collagen [14] as well as the interface interaction between bone crystal and collagen [15] on the fracture behaviour of cortical bone at the nanoscale level. At the microscale level, the impact of microstructure morphology and heterogeneity [5–7,16], the role of the osteons and the cement lines

Nomenclature		$e22_t$	threshold strain in transverse direction
		l_c	characteristic length and
$[C_d]$	material stiffness tensor	v_{12}	Poisson's ratio
E_1	longitudinal elastic modulus	δ_{eq}	current displacement value of element
E_2	transverse elastic modulus	δ_{eq}^0	displacement at initiation of stiffness degradation
G_{12}	shear modulus	δ_{eq}^f	displacement at complete damage
G_C	fracture energy	$\{\varepsilon\}$	effective strain tensor
X^S	longitudinal shear strength	ε_{eq}^f	engineering strain at complete fracture
X^T	longitudinal tensile strength	$\{\sigma\}$	Cauchy effective stress tensor
X^c	longitudinal compressive strength	σ_{11}	effective longitudinal stress
Y^C	transverse compressive strength	σ_{22}	effective transverse stress
Y^S	transverse shear strength	σ_{eq}^0	Hashin strength
Y^T	transverse tensile strength	τ_{12}	effective shear stress
d_1	damage variable in the longitudinal direction	d	damage variable
d_2	damage variable in the transverse directiom	η	viscosity parameter
d_v	viscous damage variable		
$e11_t$	threshold strain in longitudinal direction		

[10,11] and the orientation of a propagating crack [9,11] on cortical bone fracture behaviour have also been explored using such models. Despite these advances in computational modelling of cortical bone fracture, intrinsic toughening mechanisms, integral to the fracture process, have received little attention. Intrinsic toughening mechanisms act to delay the start of crack propagation [3]. Intrinsic toughening is a result of inelastic deformation mechanisms at the nano and sub-micro length scales which eventually result in the formation of a damage zone ahead of the crack tip [3]. In young healthy bone, this damage zone has been shown to consist of a diffuse form of microcracks [17,18]. The size of these diffuse microcracks are in the order of tens of microns making them smaller than the classic Frost-Burr linear microcracks [18–20]. To differentiate between these two types of microcracks, the damage zone will be referred to as the micro-damage process zone (MDPZ). The formation of this damage zone is consistent with microcracking phenomena in other materials [21]. Although, the relative importance of this damage zone to bone toughening has been questioned [3,22], other studies have argued for the significant role it plays in bone fracture resistance [18]. The formation of the MDPZ is thought to initiate by cracks nucleating between the bone crystals of the mineralised collagen [23]. The much tougher organic phase then undergoes larger scale deformation thereby inhibiting these minute cracks in the mineral phase from growing and propagating to complete fracture [24,25]. The large-scale deformation of the organics and the corresponding interaction between the crystal-organics interface are thought to dissipate a large amount of energy which would otherwise serve as the driving force for fracture [20,25].

Willett et al. [26] recently carried out a study to gain further insight into this potentially vital toughening mechanism. In this study, they imaged the MDPZ formed during fracture of single edge notched bending (SENB) specimens (cut from bovine tibia) using a barium sulphate staining technique and high resolution micro computed tomography (microCT) [26]. They found a large MDPZ of approximately 550 μm in size was formed during transverse fracture [26]. This was more than a quarter of the available unbroken
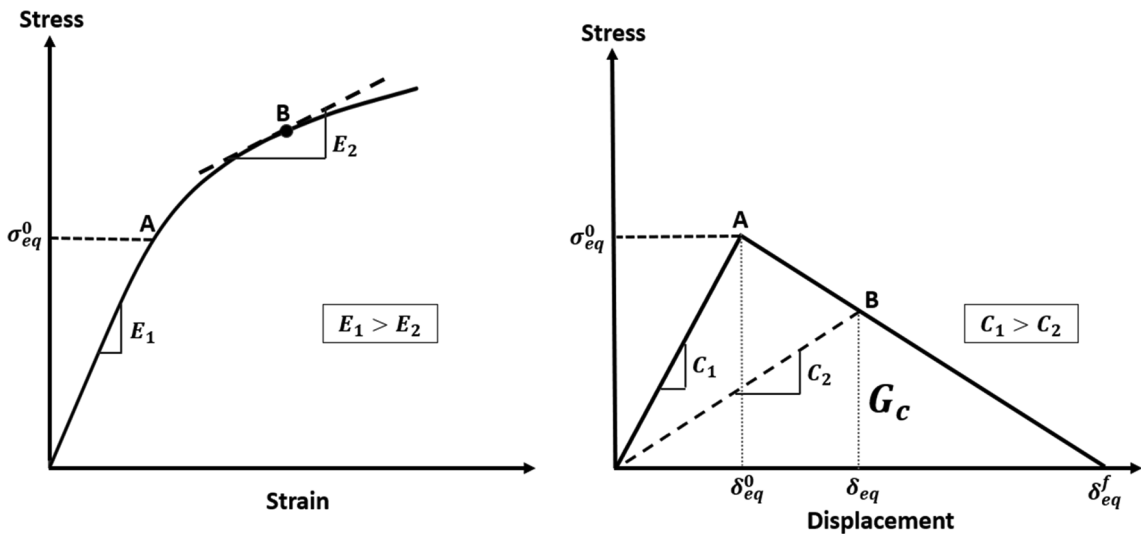

Fig. 1. (a) A representative stress-strain curve for bovine cortical bone from a longitudinal tensile test (b) A continuum damage mechanics (CDM) bi-linear law.

ligament. This suggests the significant impact the MDPZ may have on the fracture toughness of cortical bone, hence the need for further studies to better understand and model the MDPZ.

Consequently, the aim of this study was to build and validate a model that simulates the formation of the MDPZ during fracture of bovine cortical bone on the transverse plane. Since the formation of the MDPZ is a diffuse microcracking phenomenon, it was hypothesized that a continuum damage mechanics (CDM) approach would be able to adequately model the MDPZ. CDM applies mathematical models to characterise damage accumulation in materials [27], which in this study would be the accumulation of micro-damage. The accumulation of micro-damage leads to the softening of the cortical bone and therefore a reduction in its stiffness [28].

A CDM model of the MDPZ will provide further insight into the mechanisms involved in the formation of MPDZ as well as improve understanding of how changes in the mechanical competence of bone affects the formation of the MDPZ and its resultant effect in the fracture toughness of bone. Further, a CDM model could provide a means to quantity how the damage zone re-distributes stress ahead of a crack tip, which is vital to understanding mechanisms of fracture toughness and developing rigorous fracture mechanics approaches for cortical bone. Finally, a CDM model able to accurately simulate the formation of damage and fracture of cortical bone at the continuum level could find application in a broad range of biomechanics studies, including injury biomechanics (e.g. stress fractures) and orthopaedic biomechanics.

2. Theory

To model the MDPZ, the commercial finite element software ABAQUS™ was utilised. ABAQUS was used because it provides an in-built continuum damage mechanics (CDM) function for fiber reinforced composites which is applicable to modelling the MDPZ in cortical bone.

To illustrate the theory behind this, consider Fig. 1. Fig. 1a illustrates a representative stress-strain curve derived from a longitudinal tensile test for bovine cortical bone. The curve is initially linear with a constant material stiffness (E_1) but eventually becomes non-linear beyond a threshold stress (σ_{eq}^0). Studies, especially acoustic emission studies, have shown that the onset of this non-linearity in the curve coincides with the onset of microdamage formation in the bone tissue [29,30]. In other words, the onset of microdamage formation leads to softening in the bone tissue hence the non-linearity observed in the curve. This microdamage formation continues to form beyond this point until complete fracture (catastrophic failure) [26] resulting in continual material stiffness degradation observed in the stress-strain curve. Hence at point B in Fig. 1a, the instantaneous material stiffness (E_2) will be smaller than the initial constant material stiffness (E_1) [28].

To simulate the MDPZ computationally, this behaviour of material stiffness degradation with microdamage formation must be mimicked. Therefore, a bi-linear CDM law, as shown in Fig. 1b, was defined to control the local material behaviour, specifically its stiffness. The CDM law allows an initial linear elastic behaviour (constant stiffness) up to the threshold stress (σ_{eq}^0) followed by gradual stiffness degradation until failure. Hence, an element in ABAQUS, which represents the local bone material, when displaced by δ_{eq} will have a degraded stiffness of C_2. Using this stiffness degradation effect of micro-damage formation, the MDPZ during cortical bone fracture can be mapped in the computational model.

2.1. Formulating the bi-linear CDM law

In this study, cortical bone was assumed to be transversely isotropic and asymmetric in strength, therefore four CDM laws were needed to capture all possible failure modes. These were the longitudinal tension, longitudinal compression, transverse tension and transverse compression failure modes. The longitudinal direction refers to the direction parallel with the long axis of the bone and the transverse direction is perpendicular to said long axis of the bone, and in 2D directed in the circumferential direction (Fig. 2). To
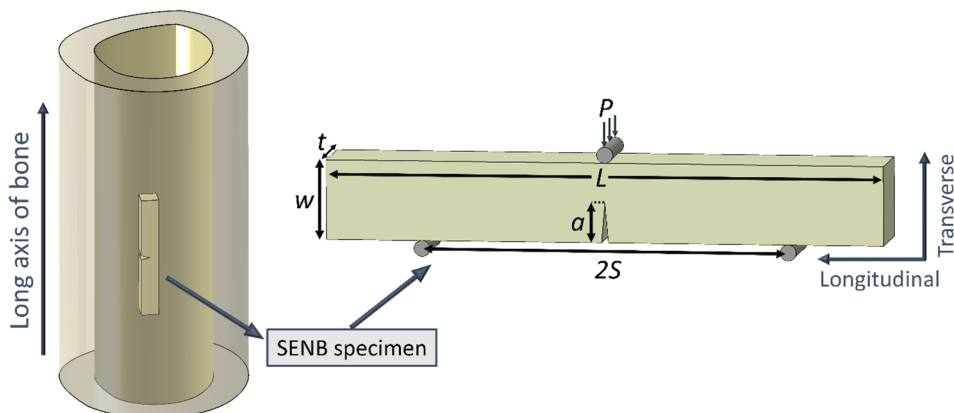

Fig. 2. Schematic illustration of a long bone diaphysis and a single edged notched bend (SENB) specimen cut from the diaphysis showing material directions and specimen dimensions.

define the CDM law for each of these failure modes, two parameters were needed, specific to the failure mode:

1. The stress at which microdamage formation initiates
2. The fracture energy

2.1.1. Microdamage formation initiation

To determine the stress at which microdamage formation initiated, the Hashin failure criteria were used [31]. The Hashin failure criteria are commonly used failure criteria for fiber reinforced composites and have previously been used when modeling bone [32]. Further, bone has been modelled as a fiber reinforced composite, where the osteons are considered the reinforcing unidirectional fibers and the extra-fibrillar matrix that surrounds the osteons considered the matrix [33]. Additionally, Hashin's criteria is available in the finite element software ABAQUS^{TM}/Standard that will be used to build the model and is coupled with the ability to simulate progressive damage. The Hashin failure criteria define failure in the four different failure modes (longitudinal tension and compression and transverse tension and compression) and are given as:

$$
\begin{aligned}
F_X^t &= (\sigma_{11}/X^T)^2 + \alpha(\tau_{12}/X^S)^2 & \sigma_{11} \geq 0 \\
F_X^c &= (\sigma_{11}/X^C)^2 & \sigma_{11} \geq 0 \\
F_Y^t &= (\sigma_{22}/Y^T)^2 + (\tau_{12}/X^S)^2 & \sigma_{22} \geq 0 \\
F_Y^c &= (\sigma_{11}/2Y^S)^2 + [(Y^C/2Y^S)^2 - 1](\sigma_{22}/Y^C)(\tau_{12}/X^S)^2 & \sigma_{22} \geq 0
\end{aligned}
\tag{1}
$$

where σ_{11}, σ_{22}, τ_{12} are the effective longitudinal, transverse and shear stresses respectively and X^T, X^c, X^S are the longitudinal tensile, compressive and shear strengths respectively, and Y^T, Y^C, Y^S are the transverse tensile, compressive and shear strengths respectively. α is a coefficient that determines the contribution of the shear stress to the longitudinal tensile initiation criterion (assumed to be $\alpha = 0$ for this model). $F_X^{t,c}$ represents the value of the failure variable in the longitudinal direction when in tension or compression, respectively, $F_Y^{t,c}$ represents the value of the failure variable in the transverse direction when in tension or compression, respectively.

With this model, failure occurs when the failure variable reaches a value of one, signifying the start of microdamage formation in that failure mode. The stresses at microdamage initiation will differ for the four failure/loading modes, explaining why four CDM bilinear laws were defined, each representing a failure mode. However, in transverse directed SENB fracture testing, the most critical loading mode will be the longitudinal tension mode (in Mode I). The stiffness before these stresses in the CDM bi linear are constant and are based on the elastic modulus for that particular loading mode and relevant directions.

2.1.2. Fracture energy

The fracture energy is the total amount of energy that is needed to completely fracture the local bone material. Inferring from this definition, the fracture energy will be equal to the area under the CDM bi-linear law. Therefore, the fracture energy ($G_{C(i)}$) for a particular failure mode is given as:

$$
G_{C(i)} = 1/2 \bullet \sigma_{eq}^0 \bullet \delta_{eq}^f
\tag{2}
$$

where σ_{eq}^0 is the Hashin strength and δ_{eq}^f is the displacement at failure for the failure mode of interest.

Knowing the variables stated in Eq. (2), the fracture energy to use for the CDM bi-linear law can be calculated. Eq. (2), however, poses a problem. Although the model has not yet been described, the CDM law will be assigned to individual elements in the model built in ABAQUS. Different sized elements will therefore have different displacements at failure. To take this into account, the displacement at failure in the equation is converted to the strain at failure. The strain at failure is fairly consistent, irrespective of element size, as fracture in cortical bone has been shown to be strain controlled [34]. This conversion is done by taking advantage of the characteristic length variable that ABAQUS assigns to every element. The characteristic length of an element in ABAQUS is dependent on the size and order of the element [35]. The characteristic length is analogous to the original length concept in calculating engineering strain. Therefore, Eq. (2) becomes:

$$
G_{C(i)} = 1/2 \bullet \sigma_{eq}^0 \bullet l_c \bullet \varepsilon_{eq}^f
\tag{3}
$$

where l_c is the characteristic length and ε_{eq}^f is the engineering strain at complete fracture.

The fracture energy can be calculated when the characteristic length of the elements as well as the Hashin strength and failure strain in the failure mode of interest are known. The CDM law can therefore be established once all these three parameters have been determined.

2.2. Stiffness evolution

Using the established CDM laws, the stiffness of the elements can be evolved to reflect the effect of microdamage formation on the bone tissue. The stiffness evolution is based on a damage variable which is defined from the CDM law (Fig. 1b) and given as [36]:

$$
d_{fm} = \frac{\delta_{eq}^f(\delta_{eq} - \delta_{eq}^0)}{\delta_{eq}(\delta_{eq}^f - \delta_{eq}^0)}
\tag{4}
$$

where d_{fm} is the damage variable, δ_{eq}^0 is the displacement at initiation of stiffness degradation, δ_{eq}^f is the displacement at complete

damage (fracture) and δ_{eq} is the current displacement of the material for the failure mode of interest

The damage variables from the different failure modes can then be incorporated into an element's stiffness tensor given as [36]:

$$C_d = \frac{1}{D} \begin{bmatrix} (1-d_1)E_1 & (1-d_1)(1-d_2)v_{21}E_1 & 0 \\ (1-d_1)(1-d_2)v_{12}E_2 & (1-d_2)E_2 & 0 \\ 0 & 0 & D(1-d_{12})G_{12} \end{bmatrix} \tag{5}$$

where $\quad D = 1 - (1-d_1)(1-d_2)v_{21}v_{21}$

$$d_1 = \begin{cases} \text{damage variable in longitudinal tension} & \sigma_{11} \geq 0 \\ \text{damage variable in longitudinal compression} & \sigma_{11} < 0 \end{cases}$$

$$d_2 = \begin{cases} \text{damage variable in transverse tension} & \sigma_{22} \geq 0 \\ \text{damage variable in transverse compression} & \sigma_{22} < 0 \end{cases}$$

$$d_{12} = 1 - (1-d_1)(1-d_2)$$

E_1, E_2 and G_{12} are the undamaged (initial) longitudinal, transverse and shear Young moduli.

v_{12} and v_{21} are the undamaged Poisson's ratios.

With the damaging stiffness matrix defined, the stress-strain response of the bone material element can be computed using [36]:

$$\{\sigma\} = [C_d]\{\varepsilon\} \tag{6}$$

A statement of Hooke's Law, where $\{\sigma\}$ is the Cauchy effective stress tensor, $[C_d]$ is the damaging stiffness tensor and $\{\varepsilon\}$ is the strain tensor.

3. Modelling in ABAQUS

3.1. Geometry, boundary conditions and meshing

Since transverse isotropy was assumed, a 2D model of a SENB bovine specimen was built in ABAQUS™/Standard. This assumption of transverse isotropy is reasonable as the mechanical properties in the circumferential and radial directions of bovine bone have been shown to match closely but are significantly different from the mechanical properties in the longitudinal direction [37,38]. The SENB specimen had dimensions 2S = 40 mm, L = 50 mm, w = t = 4 mm and a = 2 mm (See Fig. 2). A plane of symmetry was applied to the SENB bovine specimen along the transverse plane, hence only half of the specimen was modelled. A roller boundary condition and a displacement control were placed at the base and top respectively to replicate the experimental testing setup (See Figs. 2 and 3).

To reduce computational cost, a region of interest (ROI) was defined around the crack tip. The ROI was sized based on the estimated area around the crack tip that the MDPZ was expected to fill [26]. This ROI required a finer mesh than the rest of the model to accurately capture the formation of the MDPZ. The ROI as defined had a height of 2 mm and a width of 1.5 mm around the crack tip (See Fig. 3). Further, only the elements in the ROI were assigned the ability to simulate microdamage formation, also to reduce
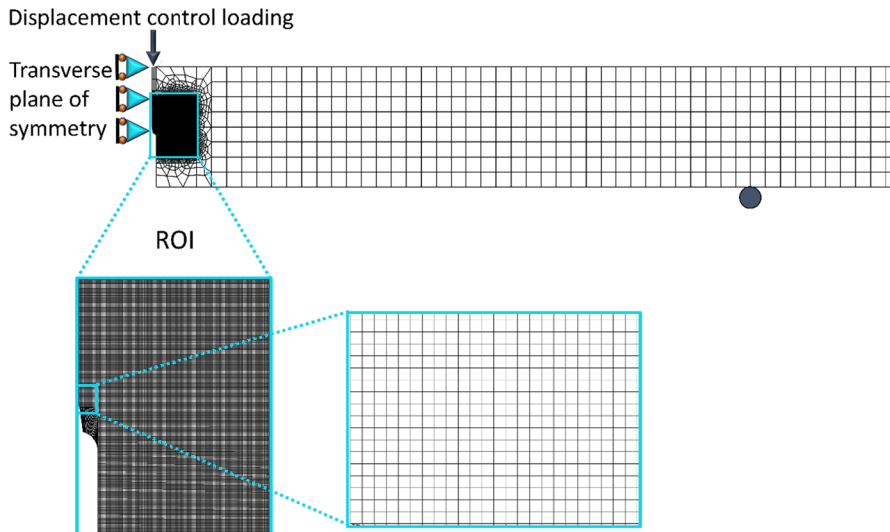

Fig. 3. Mesh pattern and region of interest (ROI) for the SENB specimen.

computation cost. The ROI was meshed with 8-node plane stress quadrilateral elements (CPS8), 10 μm in size, with the rest of the model meshed with 500 μm sized 4-node plane stress quadrilateral elements (CPS4) (Fig. 3). A mesh sensitivity study was run to ensure mesh size insensitivity.

3.2. Mechanical properties

The mechanical properties necessary for the simulation of the MDPZ were taken from Reilly and Burstein [37] and Li et al. [38]. Table 1 presents the strain values at complete fracture (ε_{eq}^f), which were used to calculate the fracture energies (Eq. (3)) for the different failure modes. Since the CDM bi-linear law is assigned to the individual elements, the fracture energy calculated is per element. The characteristic length for a second order quadratic element is half its size [35]; hence for the ROI, this was equal to 5 μm.

Due to the variability of mechanical properties of bovine bone reported in literature, even within the same study, representative values for the elastic moduli and Hashin strengths were chosen by calibrating the CDM model to match the stiffness of the specimen from the experiments. Table 2 presents typical mechanical properties used in simulating the MDPZ for bovine cortical bone.

3.3. Solution convergence

In this study, the fracture test was a quasi-static test, therefore, the CDM model was simulated in ABAQUS/Standard with approximately 1000 sub-steps. However, the CDM model simulations involved considerable non-linearity. Therefore, ABAQUS used a Newton-Raphson scheme to solve the set of non-linear stress-strain equations that were generated. However, due to the appreciable stiffness degradation that occurred, the model experienced convergence difficulties. To solve this, ABAQUS provides a viscous regularisation scheme. This scheme introduces a viscous damping effect on the damage variable, making damage, time or rate dependent. Mathematically, the damage variable is related to the new viscous damage variable by the following first order differential equation:

$$d(d_v)/dt = 1/\eta(d - d_v) \tag{7}$$

where d_v is the viscous damage variable, $d(d_v)/dt$ is the first derivative of the viscous damage variable with respect to time, d is the inviscid damage variable and η is a viscosity parameter that represents the characteristic stress relaxation time of the material.

Fondrk and co-workers [39,40] showed the necessity of viscoelastic (time dependent) behaviour in the accurate modelling of mechanical damage in cortical bone. Based on their work, the viscous regularisation scheme was used herein to introduce time dependent behaviour in the formation of the MDPZ in the CDM model. ABAQUS requires the input of the viscosity parameter (η) to define the time-dependent behaviour. The value of η was selected based on the experimental and modelling work by Fondrk and co-workers [39,40]. This is presented in the Appendix. The viscosity parameter values used in this study were between 0.07 and 0.08 s for the longitudinal direction and 0.05 s for transverse direction.

3.4. Verification of model

The bi-linear behaviour of the elements in our CDM model was verified by modeling uniaxial tensile tests on a simple plate model in both the longitudinal and transverse directions. Furthermore, a uniaxial tensile test model in the longitudinal direction was run to obtain a loading/un-loading curve in which the applied stress exceeded the Hashin strength criteria. As expected, the unloading curve returned to zero with a lesser stiffness, compared to the initial stiffness, verifying the correct behaviour of the elements.

4. Experimental validation

4.1. Specimen preparation

Experimentally generated MDPZs measured using digital image correlation (DIC) were used to validate the CDM model. Femur from a young steer (1.5–2 years old) was sourced from a local abattoir and kept frozen at −20 °C. Two SENB cortical bone samples were cut from the posterior mid-diaphysis. The sample preparation was consistent with previous works [26,41,42] and their geometry followed closely that depicted in Fig. 2. To cut the samples out of the bovine femur, the femur was rid of any soft tissue. Using a wood band saw (14″ Craftex CX104, Busy Bee tools, Canada), the posterior mid-diaphysis was isolated. A CNC mini vertical mill (Sherline, Vista, California, USA) was then used to cut out a rectangular block from the diaphysis approximately 60 mm × 15 mm × 5 mm. Utilising a combination of a low speed metallurgical saw (Isomet , Buehler, Lake Blluff, IL, USA) with a

Table 1
Strain at complete fracture in the different failure modes.

Failure mode	Failure strain
Longitudinal tension	0.02
Longitudinal compression	0.016
Transverse tension	0.007
Transverse compression	0.042

Table 2

Mechanical properties used for one of the simulations in the CDM model. X and Y represents the longitudinal and transverse strengths respectively. The superscripts T, C and S refer to tension, compression and shear respectively. The subscripts 1 and 2 represents the longitudinal and transverse directions.

Elastic moduli	Value (MPa)	Hashin Strengths	Value (MPa)	Fracture energies per element	Value (N/mm)
E_1	19,100	X^T	95	$G^T_{C(1)}$	0.00475
E_2	10,400	X^C	190	$G^C_{C(1)}$	0.0076
v_{12}	0.275	X^S	50	$G^T_{C(2)}$	0.00875
G_{12}	4100	Y^T	50	$G^C_{C(2)}$	0.011
G_{13}	4100	Y^C	105		
G_{23}	3300	Y^S	70		

300 μm diamond wafering blade (15HC diamond, Isomet, Buehler, Lake Bluff, IL, USA) and polishing by hand to a 6 μm finish, the block was divided into two rectangular beams of 50 mm × 4 mm × 4 mm (l × w × t). The polishing was carried out by initially using 8″ diameter metal bonded diamond discs (UltraPrep, Buehler, Lake Bluff, IL, USA) and finally with a polycrystalline diamond suspension (MetaDi Supreme, Buehler, Lake Bluff, IL, USA). The length was oriented along the longitudinal direction of the bone (long axis of the bone) and the thickness along the radial direction. Along the circumferential direction of the beams, a starter notch with a sharpened tip was created. The 300 μm diamond wafering blade was used to create the starter notch and an ultra-sharp razor blade (American Line, Extra Keen single edge blades) was used to create the sharpened crack tip ahead of the notch. The nominal length of the sharpened starter notch was 2 mm.

4.2. Speckling specimens for digital image correlation analysis

Prior to mechanical testing of the SENB specimens, they were soaked in a phosphate buffer solution containing 1 mM Ca^{2+} for 5 h. Immediately afterwards, the surface to be imaged for later DIC measurements was speckled using an atomiser jar filled with a high-resolution toner powder (Xerox Phaser 6000 laser toner cartridge, See Fig. 4). The size of a single toner powder was approximately 4–5 μm. A very thin layer of hair spray was applied to the surface to stick the randomised toner powder to the specimen surface.

The speckling was done to aid the digital image correlation (DIC) analysis. DIC works by comparing images taken before and after deformation of a material [43,44]. An area of interest (AOI) is selected on the reference image (image taken before deformation) and this area is divided into smaller square grids. These square grids known as subsets are made up of square matrices of individual pixels with greyscale values which characterise the subset. The various subsets are then matched to their corresponding subsets on the deformed image (image after deformation) using the greyscale values of the subset's individual pixels by means of correlation algorithms. This means for this method to accurately predict the same subset between reference and deformed image, each subset must have a unique set of greyscale values for its individual pixels. The speckle pattern created on the specimens' surface with the toner powder was performed to ensure a unique set of greyscale values were obtained for the different subsets. After there are matched, the displacement and subsequently strain across the subsets and therefore the AOI can be calculated.
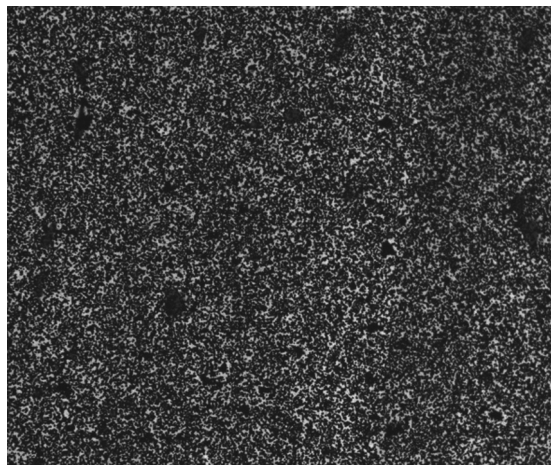

Fig. 4. A portion of the speckled surface of a bovine specimen.

4.3. Mechanical testing

After speckling, the samples underwent a three-point bending fracture test using a micro-mechanical testing system (μTS, Psylotech, Evanston, IL, USA) mounted on a vibration isolation table (Vision Isostation, Newport Corp., California, USA) (see Fig. 5). A microscope (BXFM, Olympus Corp., Center Valley, PA, USA) with a digital camera (Point Grey, 5MP, 2/3″ detector) was mounted over the test system to take magnified images of the area around the crack tip during the test. A 5x magnification objective lens (Olympus Corp., Center Valley, PA, USA) providing a 0.67 μm pixel resolution was used with the microscope. The test was run in displacement control at a rate of 0.2 mm/min with the load and load-line deflection curve recorded at a frequency of 5 Hz. The test was carried out at room temperature. The camera took images of the area around the crack tip at the same frequency of 5 Hz because it was externally triggered by the testing system.

4.4. Digital image correlation measurements of the strain fields

The images taken during the mechanical test were loaded into the DIC analysis software, Vic 2D (v6, Correlated solutions, Irmo, SC, US). This software was used to calculate strain fields based on measured displacement fields. A subset size between 81 and 100 and step size of 7 were used for the various analyses. These values are based on an internal optimisation in the software that suggests the best possible subset and step size to use. For these analyses, a zero normalised squared difference correlation criterion and an 8-tap interpolation scheme were utilised to calculate the displacements and subsequently strain. Such settings allowed for greater accuracy and dealt with any lighting differences between images [43]. To analyse the images, a large as possible AOI, ahead of the crack tip was selected and analysed for the full field strain distribution in the two material directions: longitudinal and transverse.

To aid in comparing with the CDM model, two threshold strains were defined, one for each material direction. These threshold strains were computed as:

$$e11_t = X^T / E_1 \qquad (8)$$

$$e22_t = Y^T / E_2 \qquad (9)$$

where $e11_t$ and $e22_t$ are the threshold strains in the longitudinal and transverse directions respectively, X^T and Y^T are the Hashin longitudinal and transverse tensile strengths respectively and, E_1 and E_2 are the longitudinal and transverse elastic moduli respectively.

Threshold strains between 0.45 and 0.5% were obtained. These values are consistent with strains reported in the literature at which non-linearity (micro-damage) begins in cortical bone during uniaxial tensile tests [25,45]. These regions of micro-damage defined by e11 and e22 will be referred to as the e11 micro-damage zone and e22 micro-damage zone for simplicity. Using Image J software (NIH, USA), the areas of these micro-damage zones were calculated.

To calculate the CMOD, a narrower AOI was defined such that the width just encompassed the mouth of the pre-crack created using the razor blade. This ensured the maximum displacement occurred at or very close to the crack mouth. Thus, the maximum displacement calculated using this AOI throughout the test represented the CMOD.

4.5. Validation of CDM model

To validate the CDM model in this study, outputs from the model were evaluated against their corresponding outcomes obtained experimentally. These parameters were the e11 and e22 micro-damage zone shapes and sizes, as well as the load versus load line deflection curve and load versus crack mouth opening displacement curve. For the e11 and e22 micro-damage zone shape and size, the comparison was done at defined percent secant stiffness loss points along the load–deflection curve; that is, at 5%, 10%, 15% secant stiffness losses, until the peak load (Pmax) was achieved. These percent secant stiffness losses will be referred to as P values
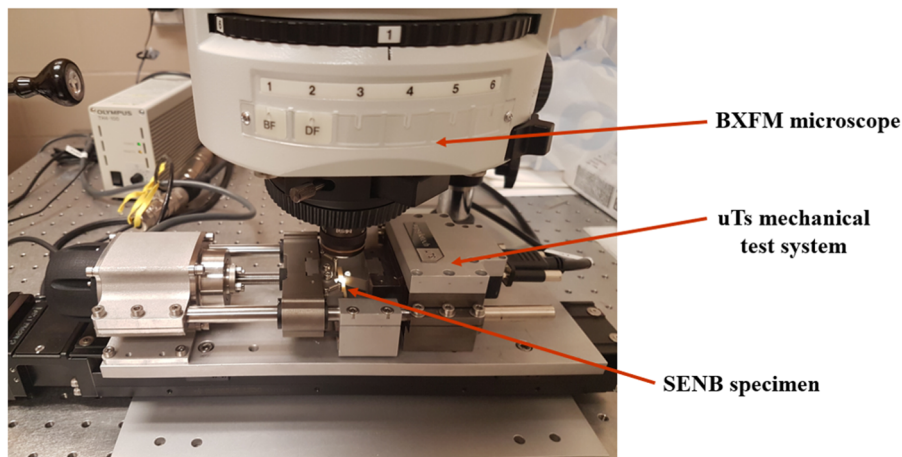

Fig. 5. A SENB specimen mounted in the Psylotech uTs mechanical testing system.
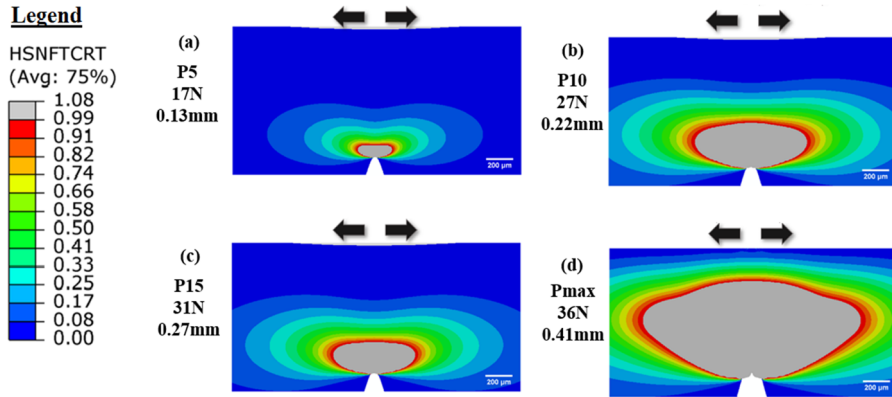
Fig. 6. The progression of the MDPZ formed in the CDM model (represented by the grey region) with increasing secant stiffness loss (represented as P value). The colour scale represents the fraction of the longitudinal tension Hashin criterion (HSNFTCRT) achieved. Elements at or exceeding 1 have met the criterion and are therefore undergoing microdamage and this is represented by the grey region as indicated by the legend. The black arrows show the direction of the far field stresses (Mode I) been considered. The load and displacement at each P value are also provided.

and this concept is derived from fracture toughness testing standards [26]. For instance, P5 stands for 5% secant stiffness loss. Pmax stands for the point at which the peak load is reached in the load-deflection curve.

To further validate the results from the CDM model, the MDPZ size (height and width) and load versus load deflection curve were compared to those obtained in Willett et al. [26] in which the MDPZ was imaged using a barium sulphate staining technique and relatively high resolution microCT.

5. Results

5.1. MDPZ from CDM model

Fig. 6 shows the progression in the formation of the model's MDPZ ahead of the crack tip with increasing load using the CDM
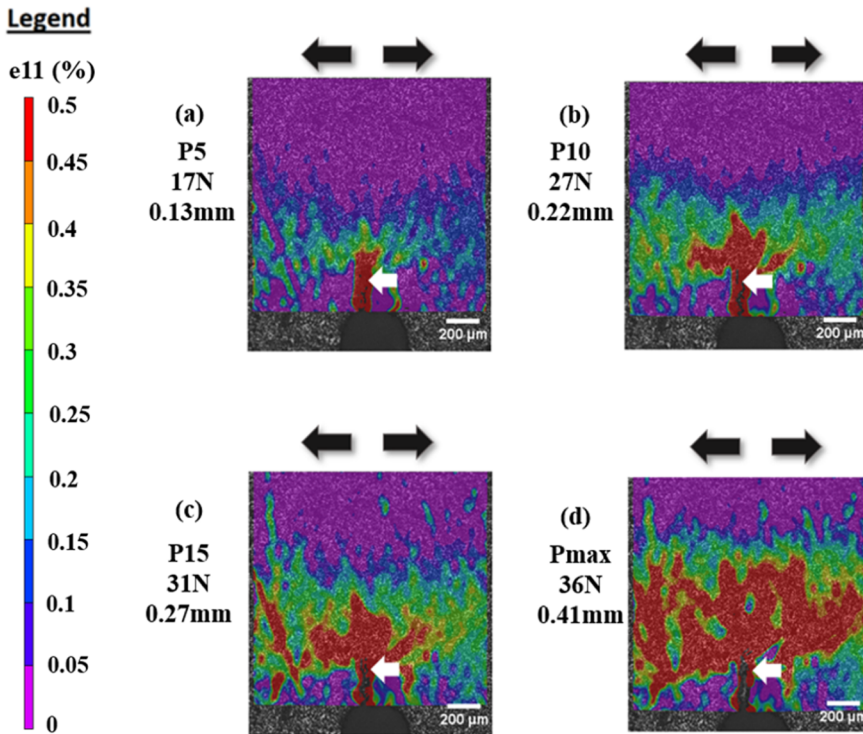

Fig. 7. The measured full field strain distributions in the longitudinal direction (e11) ahead of the crack tip with increasing secant stiffness loss (represented as P value). The red regions represent the area above the threshold strain (0.45%) in the longitudinal direction; hence, it represents the e11 micro-damage zone. The white arrows indicate the approximate location of the crack tip and the black arrows, the direction of the strain field been considered. The load and displacement at each P value are also provided.

model. The colour scale corresponds to the fraction of the longitudinal tension Hashin criterion (represented as HSNFTCRT by ABAQUS) that has been met. Elements at or exceeding 1 on this scale have therefore met the criterion and are undergoing micro-damage. Consequently, the grey region in the figure represents the MDPZ and was observed to continually increase in size with increasing P value (increasing load and loss of secant stiffness) until fracture.

5.2. CDM model validation

Fig. 7 presents the experimental DIC strain fields in the longitudinal direction, e11, for one of the bovine test specimens. The red region in the images represent the areas of strain above the threshold strain defined in Eq. (8). This red region, as stated earlier, is referred to as the e11 micro-damage zone.

Fig. 8 presents comparisons between the e11 micro-damage zones from the CDM model (grey) and experimental strain measurements (red). It was observed that there was a markedly different morphology of this damage zone between CDM model and experiment. The experimental e11 micro-damage zone was observed to be heterogenous where as the CDM model was homogenous. However, Fig. 9 shows that the size of the e11 micro-damage zones were almost identical between the CDM model and experiments. Fig. 9 also shows the size of the MDPZ defined using the longitudinal tension Hashin failure criteria, noting that the sizes of the MDPZs as defined were larger than the e11 micro-damage zones. The various micro-damage zones shown in Fig. 9 followed a second
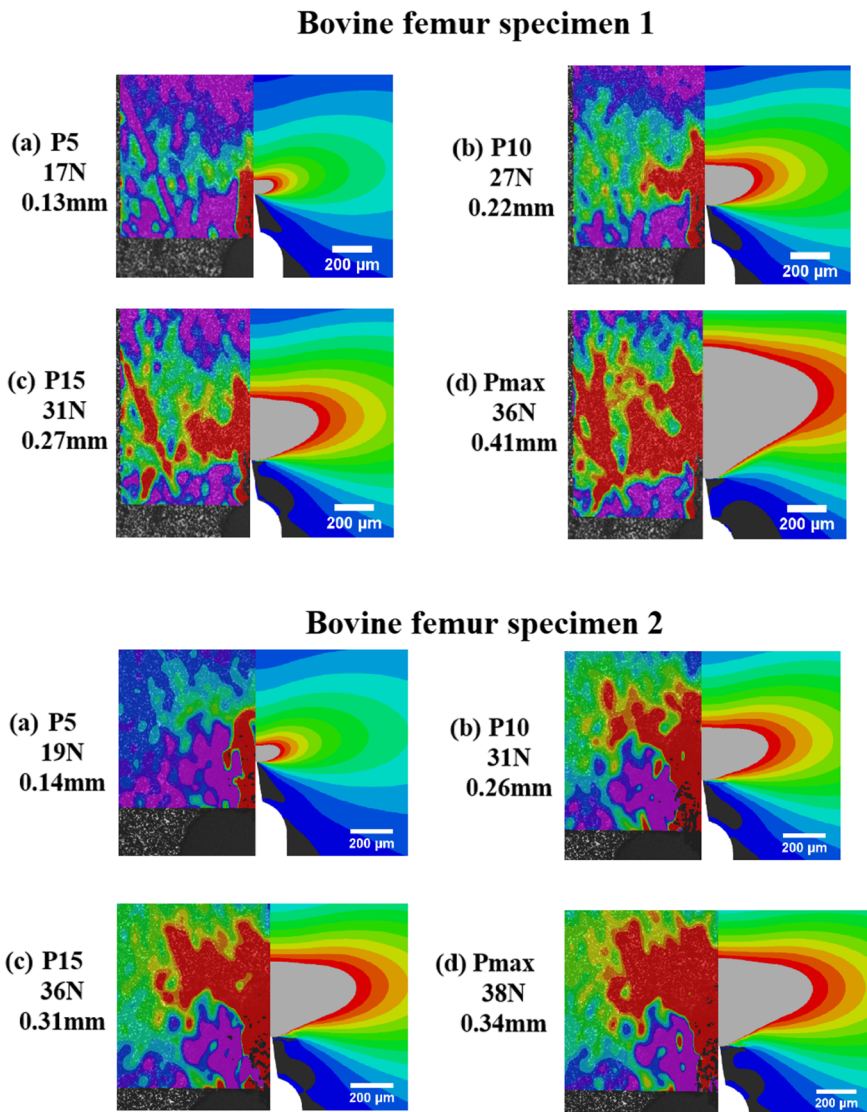

Fig. 8. Comparisons between the e11 micro-damage zones from the CDM model and from experimental DIC strain measurements for the two bovine femur specimens. The red and grey regions represent the e11 micro-damage zone for the experiments and model respectively. The experimental e11 micro-damage zone is shown on the left side and that of the CDM model on the right.
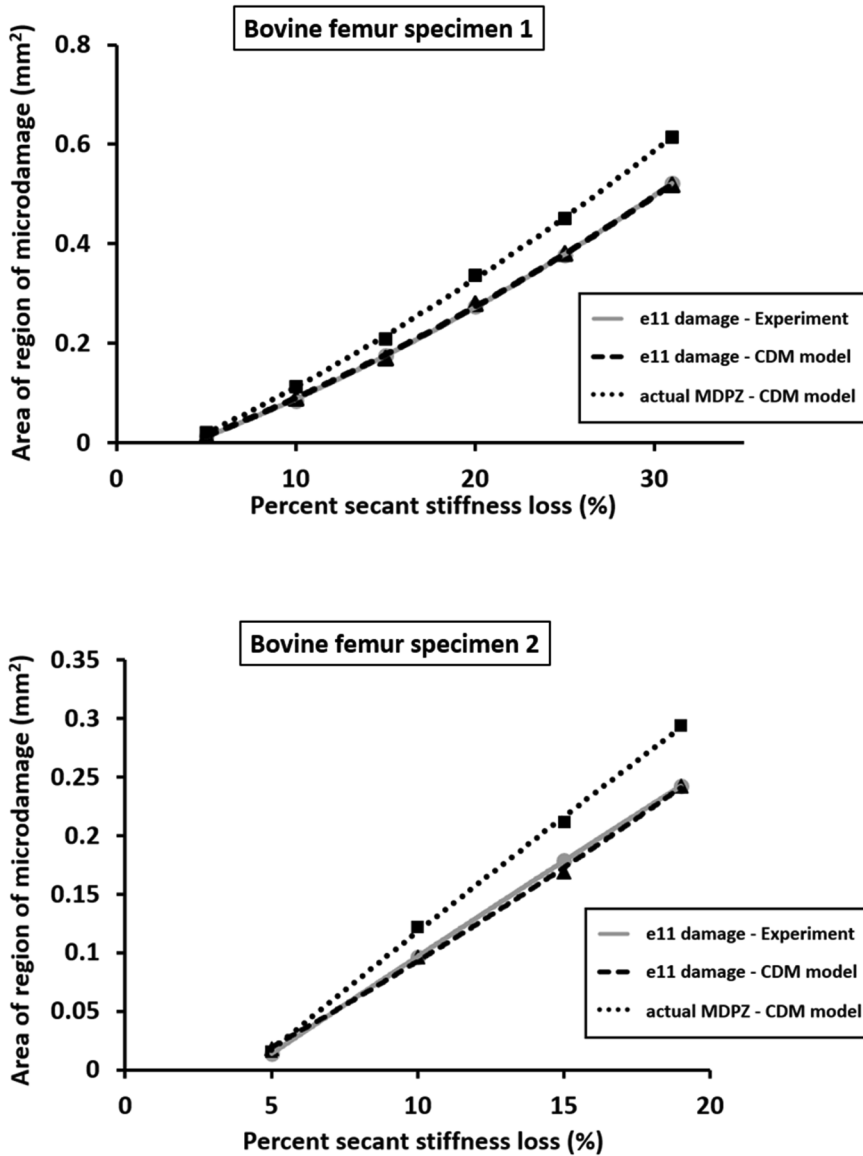
Fig. 9. Comparisons of the e11 micro-damage zone area between the CDM model and the experiments for the two bovine femur specimens.

order polynomial function with increasing P values ($R^2 \geq 0.99$). Fig. 9 further shows that the MDPZ size increased continually with no plateau up to P_{max}.
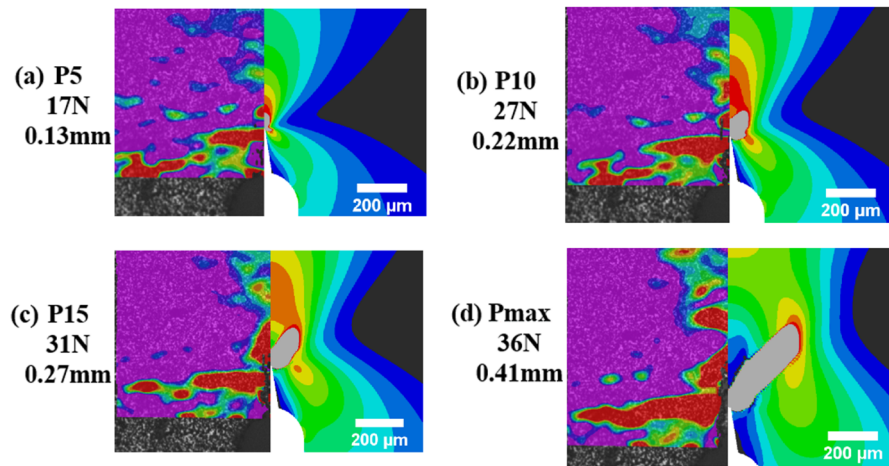
Fig. 10 presents the e22 equivalent of Fig. 8, comparing the e22 micro-damage zones of the CDM model and experiments. Again, the experiments show a heterogenous micro-damage zone whereas the CDM model provides a homogenous micro-damage zone. Comparing their sizes in Fig. 11, there were some differences between the CDM model and experimental results, particular at higher P values.

The load deflection curves from the CDM model closely replicated the experimental data (See Fig. 12). Due to poor speckling around the crack mouth of bovine femur specimen 2, the crack mouth opening displacement (CMOD) could not be determined. Fig. 13, however, shows the comparison for the CMOD for the bovine femur specimen 1. Again, the two match closely.

5.3. Comparison with previous MDPZ imaging study

Fig. 14 presents a comparison between the load deflection curves from the CDM model and one of the specimens from the study of Willett et al. [26]. The CDM model is shown to closely replicated the experimental load- deflection curve. However, from Fig. 15, although the height of the MDPZ was closely replicated, the width of the MDPZ differed significantly between CDM model and the staining and imaging experiment from Willett et al. [26].

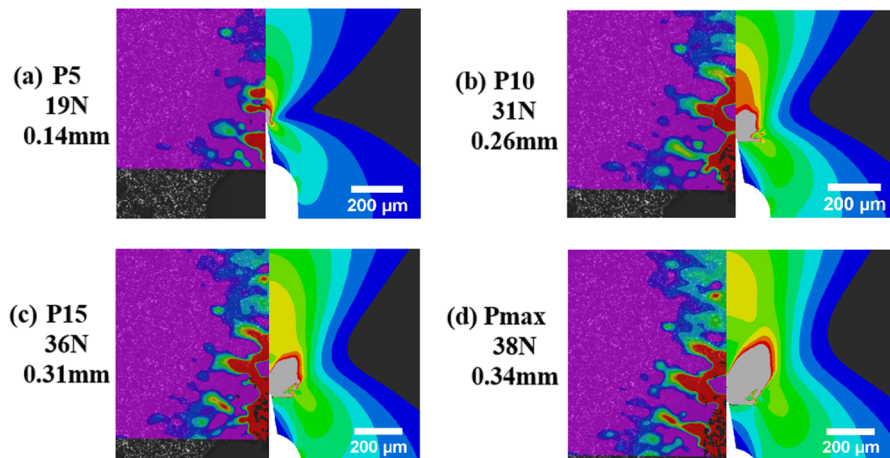## Bovine femur specimen 1

Bovine femur specimen 2

Fig. 10. Comparisons between the CDM model and experimental e22 micro-damage zones for the two bovine femur specimens. The red and grey regions represent the e22 micro-damage zone for the experiments and model respectively. The experimental e22 micro-damage zone is shown on the left side and that of the CDM model on the right.

5.4. Stress and strain along crack extension line

To understand how the stresses ahead of the crack tip are re-distributed, the stresses in the longitudinal direction were plotted against the crack extension line at different points of load represented by the percent secant stiffness loss (P values). These data are presented in Fig. 16. Fig. 17 shows the strain in the longitudinal direction along the crack extension line. It is noticed that even though the peak stresses re-distribute further away from the crack tip with increasing P values, the peak strain remains closer to the crack tip. The 0.0045 strain line drawn in Fig. 17 gives the approximate distance from the crack tip to the leading edge of the MDPZ along the crack extension line.

6. Discussion

To the best of our knowledge, this is the first experimentally validated CDM model of the MDPZ formed during transverse cortical bone fracture. The CDM model simulation as well as the DIC experiment both showed extensive formation of a MDPZ before complete fracture. This hints at how important the MDPZ is to fracture resistance in transversely directed fracture of cortical bone. The formation of a more extensive MDPZ requires more energy dissipation; energy which would otherwise serve to fuel the crack. The MDPZ blunts the stress field at the crack tip lowering the driving force.
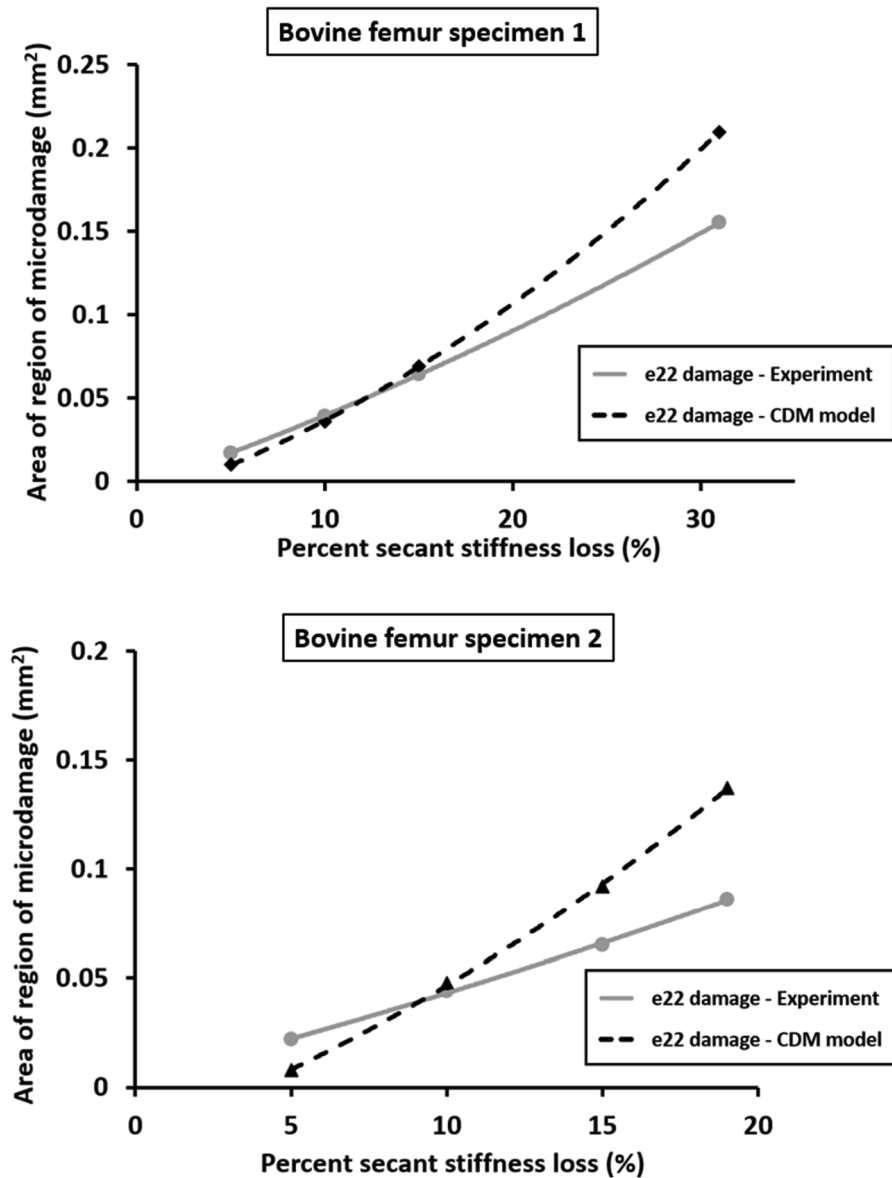
Fig. 11. Comparison of the e22 micro-damage zone areas between the CDM model and the experiment results for the two bovine femur specimens.

To validate the CDM model, parameters from the CDM model were compared to their experimental equivalents. The morphology of the e11 and e22 micro-damage process zones from the CDM model were different from the experiments (Figs. 8 and 10). This difference can be attributed to modelling cortical bone as a homogeneous continuum material in the CDM model. Despite this, the sizes of the e11 micro-damage process zones from the model and the experiments were almost identical. There were some discrepancies, however, between the model and experiment for the e22 micro-damage process zone. The reason for the discrepancy is unclear but may also be due to a lack of microstructure in the CDM model. However, the differences are minimal, and the most critical damage mode is the longitudinal tensile damage mode. This is confirmed by the fact that the e11 micro-damage process zone is about 2.5 times that of the equivalent e22 micro-damage process zone. Another important observation was that the size of the MDPZ defined using the Hashin longitudinal tension failure criteria (HSNFTCRT) was bigger than the e11 micro-damage zone for both specimens. This occurs due to strains and damage in the other directions affecting the stress achieved in the 11 direction; this is a result of Eq. (5). On the other hand, the increase in the MDPZ size with increasing P values according to a second order polynomial is consistent between the model and experiments and with reports in the literature [26]. The load versus load-line deflection curves as well as the crack mouth opening displacement curves matched very closely between CDM model and experiments. This speaks to the overall validity of the CDM model as a continuum level model. This suggests that CDM may be a relatively simple yet robust means of modelling the MDPZ that forms during bone fracture.

To match the stiffness of the experimental load versus deflection curve to its equivalent generated by the CDM model, the elastic
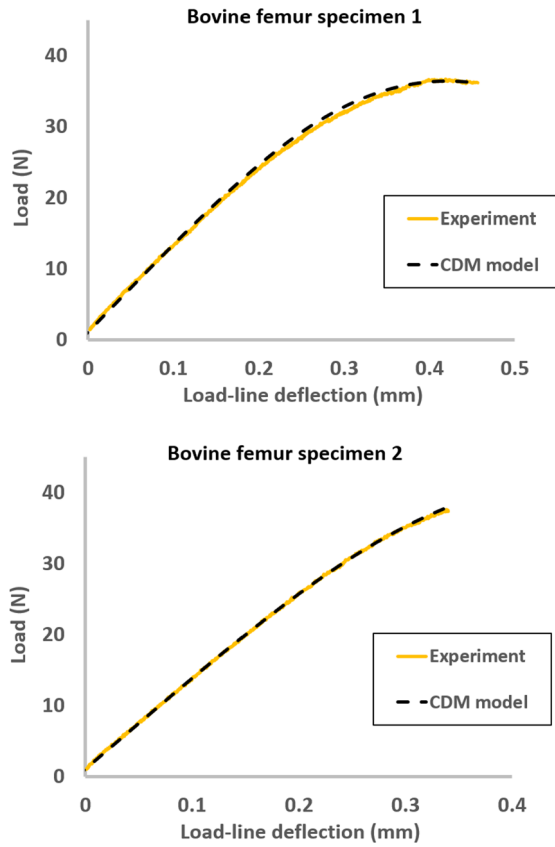
Fig. 12. Comparison of the load versus load-line deflection curves between CDM model and experiments.
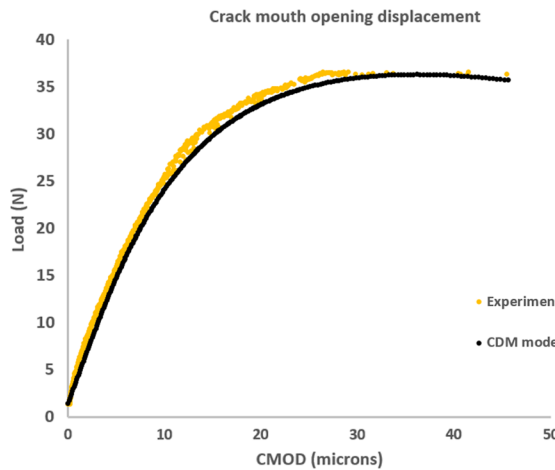

Fig. 13. Comparison of the load versus crack mouth opening displacement between CDM model and bovine femur specimen 1 experiment.

moduli of the model required calibration. The values used as reported in Table 2 compare well with the literature [37,38]. Specifically, Li and co-workers [38] reported an average longitudinal elastic modulus of 18.04 GPa and a transverse elastic modulus of 10.24 GPa for specimens taken from the posterior diaphysis of bovine femurs. These values are identical to the ones used in the CDM model herein, keeping in mind the experimental specimens were also taken form the posterior diaphysis of a bovine femur. Reilly and Burstein [37] reported an average shear modulus of 3.6 GPa for bovine cortical bone and similar values to those reported by Li and co-workers for the overall longitudinal and transverse elastic modulus. This shear modulus compares well to values used in this CDM model.

Interestingly, in comparing the MDPZ from the CDM model to the previous study in which the MDPZ was imaged using relatively
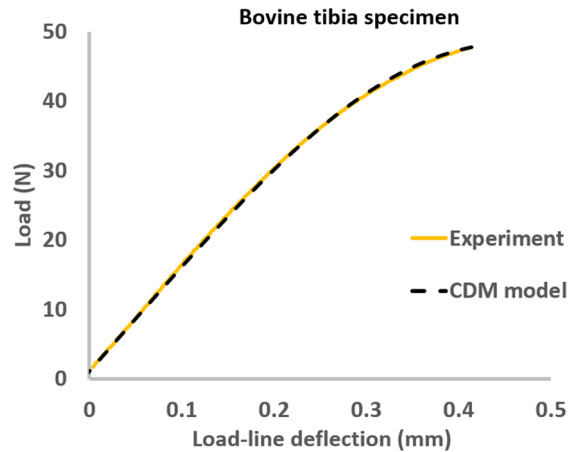
Fig. 14. Comparison of load versus deflection curves from the CDM model and the bovine tibia specimens from Willett et al. [26]
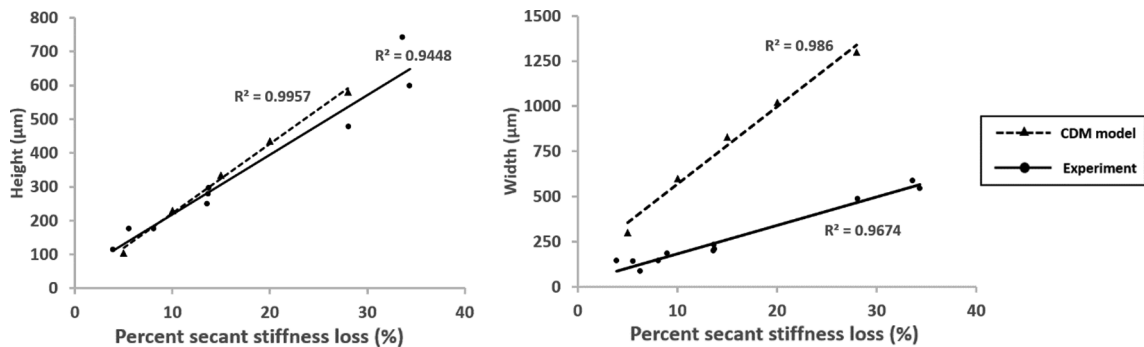

Fig. 15. Comparisons of (a) height of MDPZ and (b) width of MDPZ between the current CDM model and MDPZ imaging study from Willett et al. [26]

high-resolution micro computed tomography, the height of the MDPZ was found to be similar but the width of the MDPZ from the CDM model was much greater. It is important to note that the specimens from Willett et al. [26] had side grooves. This means that the imaged MDPZs may have been in a state of higher stress triaxiality [46] than in the current study in which side grooves would have impeded the DIC measurements. Thus, the current MDPZs from the CDM model and the DIC experiments have a lower triaxiality. Therefore, the difference in configuration may explain the disparity in the MDPZ size between the CDM model and the imaging experiment. This explanation is however made with caution. Whereas it has been clearly shown that the plastic zone (analogous to MDPZ) in relatively ductile metals differs with configuration, with a larger size for a plane stress configuration [46], this is not established in cortical bone. Further investigation into the effect of plane strain/stress configuration on MDPZ size is needed as it impacts possible standards for fracture toughness testing of cortical bone. Another possible explanation for the MDPZ size disparity may be due to the method used in the imaging study. The staining of the MDPZ was done after unloading the specimens and microdamage may close upon un-loading [47]. Furthermore, it is very possible that not all the cracks were stained by the staining technique, resulting in measurements smaller than the actual MDPZ size.

The CDM model was found to depict a stress re-distribution scheme ahead of the crack tip similar to microcracking models proposed for quasi brittle materials, such as toughened concrete [21,48] as shown in Fig. 13. Zhonghua and Yong [48] proposed an analytical microcracking model which was a modification to the LEFM based stress distribution ahead of a crack tip. This model accounts for the presence of a process zone by incorporating a cohesive zone region. Their model shows the peak stress shifting to near the tip of the process zone rather than the true crack tip, with stresses decreasing as one moves from the process zone tip back to the true crack tip. Cox and Yang [49] also showed a similar stress re-distribution along the crack extension line in their work with human cortical bone. They modelled the process zone (called a bridging zone in their work) ahead of the crack tip using a cohesive law and simulated the fracture process of cortical bone in a finite element model, which they validated against experimental load deflection curves. They stated that their model does not give any knowledge of the physical mechanisms causing the re-distribution but allude to crack bridging as a possible explanation. The CDM model presented herein however explicitly models the formation of the MDPZ and explains this stress re-distribution. The MDPZ shields the actual crack tip by limiting the peak stress and thereby delaying crack propagation. This provides further mechanistic understanding of how MDPZ formation toughens cortical bone.

Though the CDM model presented herein has been shown to be useful, verified and validated for the SENB fracture of cortical bone, it has some important limitations. In the CDM model, the Hashin failure criteria was used because bone was approximated as a
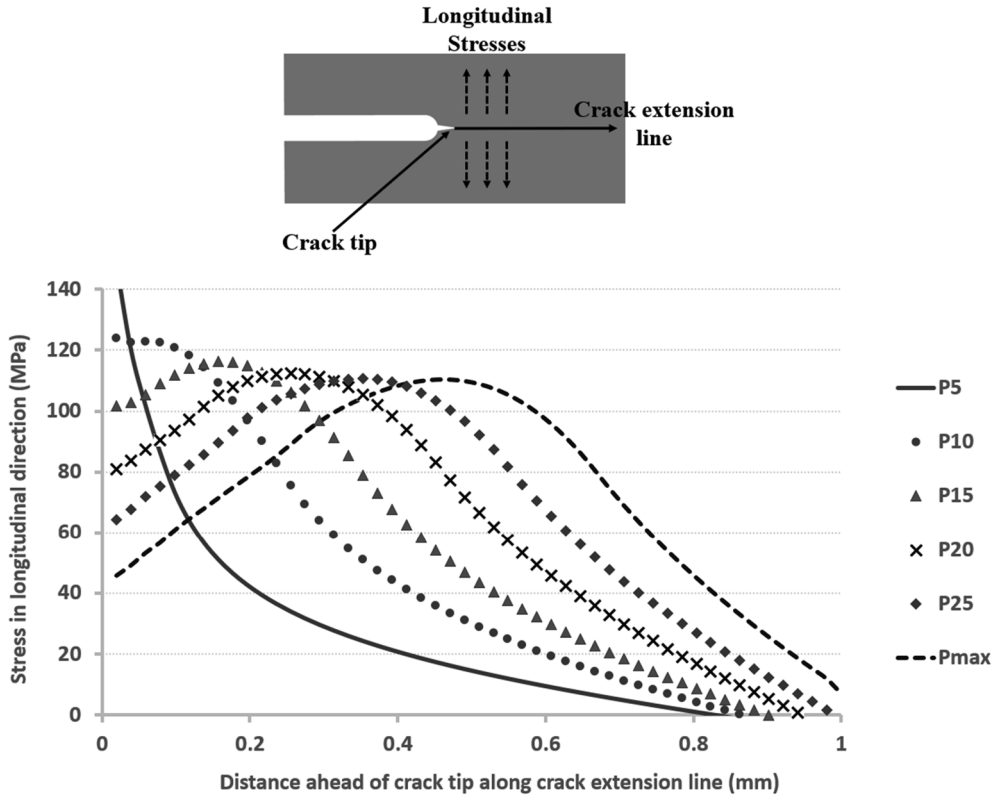
Fig. 16. Stress in the longitudinal direction along the crack extension line at different load points on the load deflection curve represented by percent secant stiffness loss (P values). The schematic above the graph illustrates the crack extension line and longitudinal stress direction.
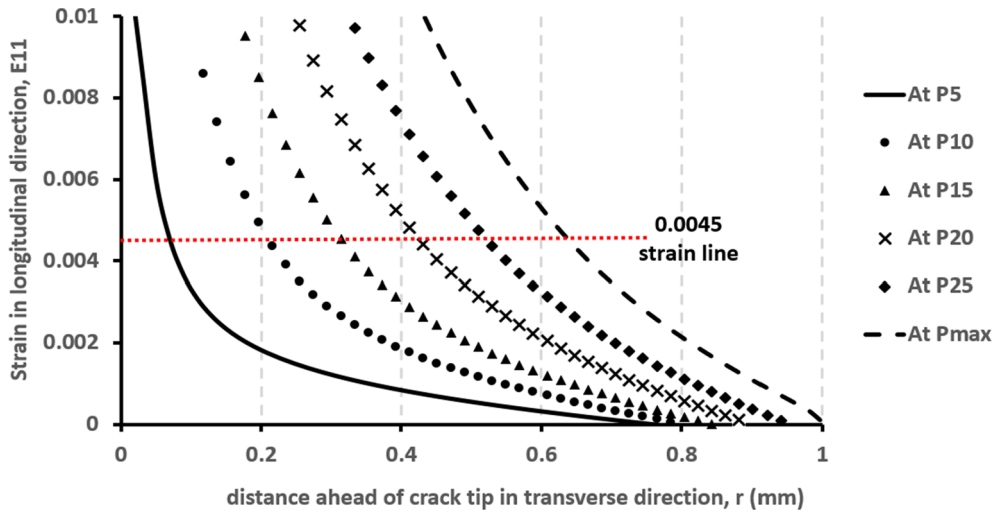

Fig. 17. Strain in the longitudinal direction along the crack extension line at different load points on the load deflection curve represented by percent secant stiffness loss (P values).

fiber-reinforced composite [33,50]. This failure criteria provided adequate results. However, it might be worthwhile to further investigate if another failure criterion can better characterise the initiation of micro-damage formation in cortical bone. Secondly, it remains a 2D model and does not incorporate stress triaxiality effects that may affect the formation of the MDPZ. On the other hand, plane strain effects on the MDPZ of cortical bone are not established, as mentioned above. Another limitation is the cortical bone material is modelled as a continuum material with no microstructure or heterogeneity. The lack of microstructure and heterogeneity likely accounts for some of the disparity between the model and experimental micro-damage zones morphologies. Such microstructure could be obtained using microcomputed tomography (microCT) or synchontron microCT and incorporated into the model.

However, this would have computational cost implications. Furthermore, plasticity is not included in this model. It is widely accepted that some level of plasticity or visco-plasticity plays a role in the bone fracture process [39]. This limitation would be especially important in simulations involving un-loading (such as cyclic loading) but is less important in this study in which unloading was not tested nor modelled (monotonic loading). Finally, a small sample size was used to validate the model and testing of more samples, as well as human bone samples, will further enhance the value of this model.

7. Conclusion

A continuum damage mechanics approach was adopted to build a model that simulates the MDPZ that forms ahead of a crack tip during the fracture of cortical bone. This study shows that CDM is a relatively simple yet robust method for modelling the MDPZ in cortical bone. The CDM model showed extensive formation of the MDPZ for a transverse directed crack in bovine cortical bone and this was validated against experimental data. The CDM model was validated against the MDPZ shape, size, load – deflection curves and crack mouth opening displacement measured in experiments. The CDM model showed a stress redistribution ahead of the crack tip similar to the stress re-distribution in the cohesive law model for human cortical bone built by Cox and Yang [49] as well as the microcracking model proposed by Zhonghua and Yong [48]. The stress re-distribution shifts the peak stress to the tip of the MDPZ, shielding the actual crack tip and delaying crack propagation. With further development of the CDM model, inclusion of heterogeneity and plasticity, and extension to human cortical bone, this tool may be valuable in gaining better mechanistic understanding of the fracture process in cortical bone especially with the formation of the MDPZ. This may potentially provide useful insights into mechanisms involved in the decreasing fracture toughness observed with age and bone damaging diseases. Furthermore, such a model would be practical for modeling damage and fracture in wholes bones when developed in 3D.

Acknowledgements

Contributions Statement

DD wrote the first draft of the manuscript and worked with the other authors (AB, JM, TW) to revise and finalize the manuscript. DD, RB and TW devised and conducted the experimental work. DD conducted the modeling with significant contributions from AB, JM and TW. TW was the principle investigator, supervised on all aspects of the research, and sought the grant funding.

Declaration of Competing Interests

None to declare for all authors.

Appendix

Fondrk et al. [39] proposed a perfectly damaging model to mimic the damage behaviour of cortical bone in tension. Although this model didn't replicate the unloading phase of the tensile behaviour of cortical bone, the loading phase was closely matched, making it a good approximation especially when considering damage in terms of loading. The perfectly damaging model works by introducing a damage and viscoelastic variable in the damage behaviour of bone. The CDM model formulation in this study therefore replicates this perfectly damaging model. The perfectly damaging model is presented in Fig. 1b and this model is analogous to the standard linear viscoelastic solid model (Fig. 1a). The viscosity parameter in the CDM formulation for the viscoelastic effect therefore represents the relaxation time of the perfectly damaging model. This is defined when no damage has occurred.

In the CDM model, the application of the displacement to the SENB specimen was run in small numerous steps. This meant within
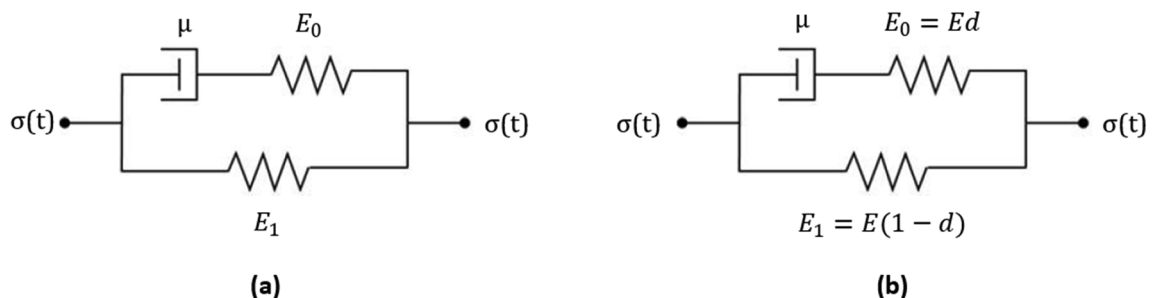

Fig. 1a. representation of the standard linear viscoelastic solid (SLS) model, and (b) representation of the perfectly damaging model proposed by Fondrk et al.[39] represents the damage variable.

each step due to the presence of time dependent behaviour, a stress relaxation response was achieved hence a constant strain condition was imposed. Considering this constant strain condition, the relaxation time for the stress relaxation response of a standard linear viscoelastic solid can given as [51]:

$$\tau = \frac{\mu}{E_0} \tag{11}$$

where μ is the viscosity co-efficient of the material/system.

Therefore, for the perfectly damaging model, the viscosity parameter (η) is also given as:

$$\eta = \frac{\mu}{E_0} \tag{21}$$

For bovine cortical bone, Fondrk et al. [39,40] found E_1, which is known as the relaxed modulus to be $0.88 \pm 0.03E^0$ where E^0 is the instantaneous (initial) elastic modulus.

From the standard linear viscoelastic solid model formulation at equilibrium [51],

$$E^0 = E_0 + E_1 \tag{33}$$

Therefore, $E_0 = 0.12 \pm 0.03E^0$ for cortical bone once relaxed to equilibrium. Also, the viscosity co-efficient (μ) was reported to be 103.5 MPa.s [39]. There is evidence that viscoelastic properties of bone are isotropic for low frequencies which approximates a quasi-static test [52,53]. Based on this assumption, the viscosity parameter was calculated for the longitudinal direction using the above equations and also used for the transverse direction. Using an average longitudinal elastic modulus of 18.7GPa, a viscosity parameter range between 0.04 and 0.07 s was obtained. A similar trial and error optimisation technique used for the other mechanical properties was used to select the specific value from the above ranges to be used in the CDM simulations.

Appendix A. Supplementary material

Supplementary data to this article can be found online at https://doi.org/10.1016/j.engfracmech.2019.106811.

References

[1] Olszta MJ, Cheng X, Jee SS, Kumar R, Kim YY, Kaufman MJ, et al. Bone structure and formation: A new perspective. Mater Sci Eng R Rep 2007;58:77–116. https://doi.org/10.1016/j.mser.2007.05.001.
[2] Ritchie RO, Buehler MJ, Hansma P. Plasticity and toughness in bone. Phys Today 2009;62:41–7. https://doi.org/10.1063/1.3156332.
[3] Launey Maximilien E, Buehler Markus J, Ritchie Robert O. On the mechanistic origins of toughness in bone. Annu. Rev. Mater. Res. 2010;40(1):25–53. https://doi.org/10.1146/annurev-matsci-070909-104427.
[4] Brodland GW. How computational models can help unlock biological systems. Semin Cell Dev Biol 2015;47–48:62–73. https://doi.org/10.1016/j.semcdb.2015.07.001.
[5] Abdel-Wahab AA, Maligno AR, Silberschmidt VV. Micro-scale modelling of bovine cortical bone fracture: Analysis of crack propagation and microstructure using X-FEM. Comput Mater Sci 2012;52:128–35. https://doi.org/10.1016/j.commatsci.2011.01.021.
[6] Budyn E, Hoc T, Jonvaux J. Fracture strength assessment and aging signs detection in human cortical bone using an X-FEM multiple scale approach. Comput Mech 2008;42:579–91. https://doi.org/10.1007/s00466-008-0283-1.
[7] Li S, Abdel-Wahab A, Demirci E, Silberschmidt VV. Fracture process in cortical bone: X-FEM analysis of microstructured models. Int J Fract 2013;184:43–55. https://doi.org/10.1007/s10704-013-9814-7.
[8] Ural A, Vashishth D. Cohesive finite element modeling of age-related toughness loss in human cortical bone. J Biomech 2006;39:2974–82. https://doi.org/10.1016/j.jbiomech.2005.10.018.
[9] Ural A. Cohesive modeling of bone fracture at multiple scales. Procedia Eng 2011;10:2827–32. https://doi.org/10.1016/j.proeng.2011.04.470.
[10] Mischinski S, Ural A. Finite element modeling of microcrack growth in cortical bone. J Appl Mech 2011;78:041016 https://doi.org/10.1115/1.4003754.
[11] Mischinski S, Ural A. Interaction of microstructure and microcrack growth in cortical bone: A finite element study. Comput Methods Biomech Biomed Engin 2013;16:81–94. https://doi.org/10.1111/anae.12598.
[12] Buehler MJ. Atomistic and continuum modeling of mechanical properties of collagen: Elasticity, fracture, and self-assembly. J Mater Res 2006;21:1947–61. https://doi.org/10.1557/jmr.2006.0236.
[13] Libonati F, Nair AK, Vergani L, Buehler MJ. Fracture mechanics of hydroxyapatite single crystals under geometric confinement. J Mech Behav Biomed Mater 2013;20:184–91. https://doi.org/10.1016/j.jmbbm.2012.12.005.
[14] Barkaoui A, Bettamer A, Hambli R. Failure of mineralized collagen microfibrils using finite element simulation coupled to mechanical quasi-brittle damage. Procedia Eng 2011;10:3185–90. https://doi.org/10.1016/j.proeng.2011.04.526.
[15] Luo Q, Nakade R, Dong X, Rong Q, Wang X. Effect of mineral-collagen interfacial behavior on the microdamage progression in bone using a probabilistic cohesive finite element model. J Mech Behav Biomed Mater 2011;4:943–52. https://doi.org/10.1016/j.jmbbm.2011.02.003.
[16] Raeisi Najafi A, Arshi AR, Eslami MR, Fariborz S, Moeinzadeh MH. Micromechanics fracture in osteonal cortical bone: A study of the interactions between microcrack propagation, microstructure and the material properties. J Biomech 2007;40:2788–95. https://doi.org/10.1016/j.jbiomech.2007.01.017.
[17] Vashishth D, Koontz J, Qiu SJ, Lundin-Cannon D, Yeni YN, Schaffler MB, et al. In vivo diffuse damage in human vertebral trabecular bone. Bone 2000;26:147–52. https://doi.org/10.1016/S8756-3282(99)00253-7.
[18] Vashishth D. Hierarchy of bone microdamage at multiple length scales. Int J Fatigue 2007;29:1024–33. https://doi.org/10.1016/j.ijfatigue.2006.09.010.
[19] Diab T, Vashishth D. Morphology, localization and accumulation of in vivo microdamage in human cortical bone. Bone 2007;40:612–8. https://doi.org/10.1016/j.bone.2006.09.027.
[20] Poundarik AA, Vashishth D. Multiscale imaging of bone microdamage. Connect Tissue Res 2015;56:87–98. https://doi.org/10.3109/03008207.2015.1008133.
[21] Carpinteri A. Nonlinear Crack Models for Nonmetallic Materials. Boston: Kluwer Academic Publishers; 1999.
[22] Nalla RK, Kruzic JJ, Ritchie RO. On the origin of the toughness of mineralized tissue : microcracking or crack bridging ? Bone 2004;34:790–8. https://doi.org/10.1016/j.bone.2004.02.001.
[23] Poundarik AA, Diab T, Sroga GE, Ural A, Boskey AL, Gundberg CM, et al. Dilatational band formation in bone. Proc Natl Acad Sci 2012;109:19178–83. https://doi.org/10.1073/pnas.1201513109.

[24] Gupta HS, Wagermaier W, Zickler GA, Ben Aroush DR, Funari SS, Roschger P, et al. Nanoscale deformation mechanisms in bone. Nano Lett 2005;5:2108–11. https://doi.org/10.1021/nl051584b.
[25] Gupta HS, Wagermaier W, Zickler GA, Hartmann J, Funari SS, Roschger P, et al. Fibrillar level fracture in bone beyond the yield point. Int J Fract 2006;139:425–36. https://doi.org/10.1007/s10704-006-6635-y.
[26] Willett T, Josey D, Xing R, Lu Z, Minhas G, Montesano J. The micro-damage process zone during transverse cortical bone fracture : No ears at crack growth initiation. J Mech Behav Biomed Mater 2017;74:371–82. https://doi.org/10.1016/j.jmbbm.2017.06.029.
[27] Lemaitre J, Desmorat R. Engineering Damage Mechanics. Berlin: Springer; 2005.
[28] Cowin SC, editor. Bone Mechanics Handbook. 2nd ed. CRC Press LLC; 2001.
[29] Wright TM, Vosburgh F, Burstein AH. Permanent deformation of compact bone monitored by acoustic emission. J Biomech 1981;14:405–9. https://doi.org/10.1016/0021-9290(81)90058-0.
[30] Zioupos P, Currey JD, Sedman AJ. An examination of the micromechanics of failure of bone and antler by acoustic emission tests and laser scanning confocal microscopy. Med Eng Phys 1994;16:203–12. https://doi.org/10.1016/1350-4533(94)90039-6.
[31] Hashin Z. Failure criteria for unidirectional fibre composites. J Appl Mech 1980;47:329–34.
[32] Feerick EM, Cheryl X, Mcgarry P. Anisotropic mode-dependent damage of cortical bone using the extended finite element method (XFEM). J Mech Behav Biomed Mater 2013;20:77–89. https://doi.org/10.1016/j.jmbbm.2012.12.004.
[33] Katz LJ. Anisotropy of Young's modulus of bone. Nature 1980;283.
[34] Nalla RK, Kinney JH, Ritchie RO. Mechanistic fracture criteria for the failure of human cortical bone. Nat Mater 2003;2. https://doi.org/10.1038/nmat832.
[35] Abaqus/Standard User's guide. BS Simulia; 2016.
[36] Lapczyk I, Hurtado JA. Progressive damage modeling in fiber-reinforced materials. Compos Part A Appl Sci Manuf 2007;38:2333–41. https://doi.org/10.1016/j.compositesa.2007.01.017.
[37] Reilly DT, Burstein AH. The elastic and ultimate properties of compact bone tissue. J Biomech 1975:393–405.
[38] Li S, Demirci E, Silberschmidt VV. Variability and anisotropy of mechanical behavior of cortical bone in tension and compression. J Mech Behav Biomed Mater 2013;21:109–20. https://doi.org/10.1016/j.jmbbm.2013.02.021.
[39] Fondrk MT, Bahniuk EH, Davy DT. A damage model for nonlinear tensile behavior of cortical bone. J Biomech Eng 1999;121:533–41. https://doi.org/10.1115/1.2835084.
[40] Fondrk M, Bahniuk E, Davy DT, Michaels C. Some viscoplastic characteristics of bovine and human cortical bone. J Biomech 1988;21:623–30. https://doi.org/10.1016/0021-9290(88)90200-X.
[41] Willett TL, Burton B, Woodside M, Wang Z, Gaspar A, Attia T. γ-Irradiation sterilized bone strengthened and toughened by ribose pre-treatment. J Mech Behav Biomed Mater 2015;44:147–55. https://doi.org/10.1016/j.jmbbm.2015.01.003.
[42] Woodside M, Willett TL. Elastic – plastic fracture toughness and rising J R -curve behavior of cortical bone is partially protected from irradiation – sterilization-induced degradation by ribose protectant. J Mech Behav Biomed Mater 2016;64:53–64. https://doi.org/10.1016/j.jmbbm.2016.07.001.
[43] Pan B, Qian K, Xie H, Asundi A. Two-dimensional digital image correlation for in-plane displacement and strain measurement : a review. Meas Sci Technol 2009;20:1–17. https://doi.org/10.1088/0957-0233/20/6/062001.
[44] Yoneyama S. Basic principle of digital image correlation for in-plane displacement and strain measurement. Adv Compos Mater 2016;25:105–23. https://doi.org/10.1080/09243046.2015.1129681.
[45] Budyn E, Hoc T. Modelling of diffuse damage near micro cracks in human cortical bone. ASME Conf. Eng. Syst. Des. Anal. 2012:1–8.
[46] Anderson TL. Fracture mechanics: Fundamentals and Applications. Boca Raton: CRC Press LLC; 2005.
[47] Currey JD. The structure and mechanics of bone. J Mater Sci 2012;47:41–54. https://doi.org/10.1007/s10853-011-5914-9.
[48] Zhonghua L, Yong Z, Schmauder S. A cohesion model of microcrack toughening. Eng Fract Mech 1993;44:257–65. https://doi.org/10.1016/0013-7944(93)90050-3.
[49] Cox BN, Yang Q. Cohesive zone models of localization and fracture in bone. Eng Fract Mech 2007;74:1079–92. https://doi.org/10.1016/j.engfracmech.2006.12.024.
[50] Fatima M, Canhao H, Eurico J. Bone: a composite natural material. Adv Compos Mater - Anal Nat Man-Made Mater 2011. https://doi.org/10.5772/17523.
[51] Pruitt LA, Chakravartula AM. Mechanics of biomaterials: fundamental principles for implant design. New York: Cambridg University Press; 2011.
[52] Abdel-Wahab AA, Alam K, Silberschmidt VV. Analysis of anisotropic viscoelastoplastic properties of cortical bone tissues. J Mech Behav Biomed Mater 2011;4:807–20. https://doi.org/10.1016/j.jmbbm.2010.10.001.
[53] Iyo T, Maki Y, Sasaki N, Nakata M. Anisotropic viscoelastic properties of cortical bone. J Biomech 2004;37:1433–7. https://doi.org/10.1016/j.jbiomech.2003.12.023.